Aspect ratio influence on the vortex induced vibrations of a pivoted finite height cylinder at low Reynolds number

J.C. Cajas [a,*], I. Rodríguez[c], E. Salcedo[a], O. Lehmkuhl[b], G. Houzeaux[b], and C. Treviño[a,d]

[a] ***ENES - Unidad Mérida, Universidad Nacional Autónoma de México, Mérida, Yucatán, México.***
[b] ***Barcelona Supercomputing Center (BSC), Barcelona, Spain.***
[c] ***Turbulence and Aerodynamics Research Group (TUAREG). Universitat Politècnica de Catalunya, Terrassa, Barcelona, Spain.***
[d] ***UMDI, Facultad de Ciencias, Universidad Nacional Autónoma de México, Sisal, Yucatán, México.***

Abstract

The effect of the aspect ratio on the vortex induced vibrations (VIV) of a pivoted finite length circular cylinder is investigated. A fixed value of the Reynolds number $Re = 100$ with four values of the aspect ratio $AR = 2$, 3, 5, 7 are considered. Different values of the reduced velocity u_r^* in the range $2 \leq u_r^* \leq 11$ were used for each AR value. Results on the oscillatory response of the cylinder, hydrodynamic forces, and wake structures are reported. In order to compare the VIV of the different length cylinders, the displacement of the center of mass (which coincides on each case) was analyzed. It is found that the maximum oscillation amplitudes, the extent of the synchronization region and the wake structures are influenced by the aspect ratio. Also, a steady symmetrical flow is obtained for the small $AR = 2$, 3 cases with relatively low values of u_r^*, which is found to be unstable when increasing u_r^*.

Keywords: Vortex induced vibrations; aspect ratio; computational fluid

*Corresponding author
Email addresses: carlos.cajas@enesmerida.unam.mx (J.C. Cajas), ivette.rodriguez@upc.edu (I. Rodríguez), erick.salcedo@enesmerida.unam.mx (E. Salcedo), oriol.lehmkuhl@bsc.es (O. Lehmkuhl), guillaume.houzeaux@bsc.es (G. Houzeaux), ctrev05@gmail.com (and C. Treviño)

dynamics; fluid-structure interaction; pivoted cylinder

1. Introduction

Vortex induced vibrations (VIV) of bluff bodies immersed in currents of fluids have been extensively investigated, reviews and books that give an excellent landscape of the development of the particular VIV field together with the general fluid-structure interaction (FSI) field can be found in [1], [2], [3], [4], [5]. Over the last years, great efforts have been devoted to the study of VIV of circular cylinders from an experimental perspective in [2], [6], [7], but also with a numerical approach [8], [9], [10], [11] [12] achieving significant advances in the understanding of VIV through these studies.

A very important feature is the existence of response branches of the VIV of circular cylinders depending on the type of mounting system, its number of degrees of freedom (dof), and the relevant physical parameters: mass of the system, natural frequency of the structure, geometrical characteristics, velocity of the current and damping parameters. Different oscillation amplitudes are observed in each branch as a consequence of the synchronization of the vortex shedding frequency and the natural frequency of the cylinder. The maximum oscillation amplitude obtained in each branch, and the determination of the parameters that influence its extension are of utmost importance to fully understand the VIV process.

Given that differences in the vortex shedding frequencies of circular cylinders have an important effect on their VIV, it is expected that variations in the aspect ratio (AR=length/diameter) of finite cylinders have a strong influence on the VIV. For example, in fixed finite circular cylinders, it has been reported that different aspect ratios induce different shedding frequencies and wake structures [13], and that inclination angle influences the vortex shedding frequency for finite cylinders of $AR = 3$ [14].

In the VIV context, finite length circular cylinders have been studied recently and the effect of aspect ratio has also been considered. Zhao and Cheng [15] investigated the 1dof VIV of a rigid circular cylinder of finite length in a uniform steady flow; the authors considered a cantilever configuration for the cylinder with a single free end. Results of the oscillation amplitudes, oscillation frequencies, wake structures and the extension of the synchronization regions were obtained. Also, supression of the shedding and VIV was observed for small values of AR. Azadeh-Ranjbar et al. [16] experimentally studied the VIV of finite length rigid circular cylinders with two free-ends attached to an elastic cantilever beam. Different aspect ratios were tested and the authors obtained a very important increment in the oscillation amplitude by reducing the aspect ratio of the cylinder.

The present manuscript addresses the effect of the aspect ratio on the VIV of a pivoted finite length cicular cylinder in the laminar regime. This configuration has received relatively little attention, and the effect of geometrical parameters on the VIV process remains to be determined. The organization of the manuscript follows: section 2 presents the system under consideration and the mathematical framework used; section 3 presents the numerical techniques, grid sensitivity analysis and numerical details; section 4 includes the results and discussion obtained from the numerical simulations and section 5 gathers the conclusions of the present work.

2. Problem Statement

The system under study is shown in Figure 1. It consists of a rigid cylindrical mast attached to a torsion spring through a thin rod. The spring is connected to a fixed base, creating a pivoted configuration. Different aspect ratios length/diameter for the mast are considered $AR = l/d = 2, 3, 5, 7$. The length of the rod supporting the cylinder is chosen to have the center of mass of

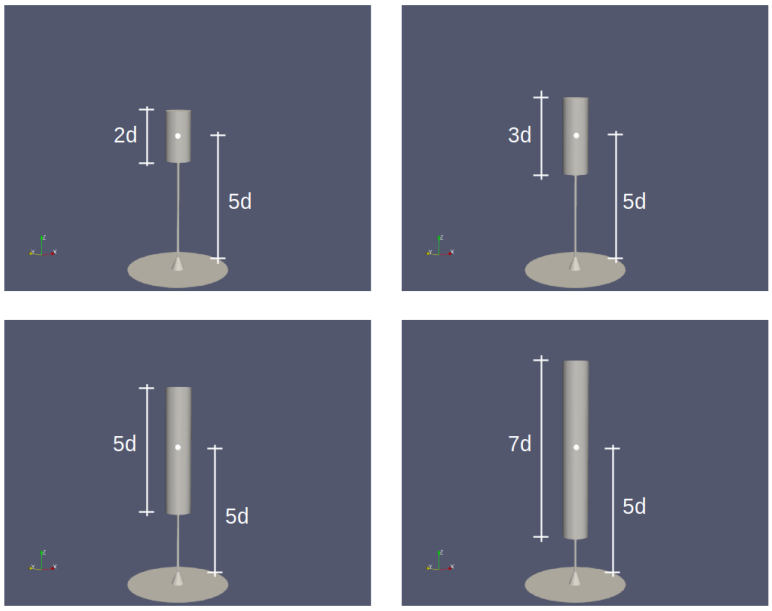

Figure 1: Sketch of the cylinders used in the present study. The aspect ratios analyzed are $AR = 2$, $AR = 3$, $AR = 5$, and $AR = 7$.

the cylinder at the same height for all aspect ratios. The mast is embedded in a Newtonian viscous fluid that flows with constant velocity u_0 upstream from the mast. The fluid is considered to be incompressible and to have constant physical properties. The computational domain is a box of 22d in the cross-flow direction, 45d in the streamwise direction, and 20d in the vertical direction. The mast is located at 10d from the box entrance. The Reynolds numbers considered is $Re = \rho_f \, u_o \, d/\mu_f = 100$, here ρ_f is the fluid density and μ_f the fluid viscosity.

2.1. Non-dimensional equations

The derivation of the set of non-dimensional equations can be found in [12]. For completeness, the equations are included here but the details are not repeated, the interested reader is invited to consult the mentioned reference. Selecting the diameter of the mast d as unit length, and the magnitude of the inflow velocity in the $x-$direction u_0 as unit velocity, the non-dimensional variables for time, coordinates, and velocities are defined: $t^* = u_0 \, t/d$, $x^* = x/d$,

$y^* = y/d$, $z^* = z/d$, $\boldsymbol{u}^* = \boldsymbol{u}/u_0$. With these variables the continuity equation and the Navier-Stokes equations are casted in non-dimensional form as follows

$$\nabla \cdot \boldsymbol{u}_f^* = 0, \tag{1}$$

$$\frac{\partial \boldsymbol{u}_f^*}{\partial t^*} + [(\boldsymbol{u}_f^* - \boldsymbol{u}_m^*) \cdot \nabla]\boldsymbol{u}_f^* - \frac{1}{Re}\nabla^2 \boldsymbol{u}_f^* + \nabla p^* = \boldsymbol{f}^*, \tag{2}$$

The angular equations of motion for the structure are

$$\begin{aligned} \ddot{\theta} - \dot{\phi}^2 \sin\theta\cos\theta + \frac{\cos\theta\cos\phi}{m_{gr}^*} - \left(\frac{2\pi}{u_r^*}\right)^2 (\sin\theta\cos\theta\cos^2\phi) - \\ \frac{2}{\pi m_r^*}(C_z\cos\theta - C_x\sin\theta) + \frac{4\pi\zeta_\theta^*\dot{\theta}}{u_r^*} = 0, \\ \sin^2\theta\,\ddot{\phi} + 2\sin\theta\cos\theta\dot{\theta}\dot{\phi} - \frac{\sin\theta\sin\phi}{m_{gr}^*} + \left(\frac{2\pi}{u_r^*}\right)^2 (\sin\phi\cos\phi\sin^2\theta) + \\ \frac{2}{\pi m_r^*}(C_z\sin\phi + C_y\cos\phi) + \frac{4\pi\zeta_\phi^*\dot{\phi}}{u_r^*} = 0. \end{aligned} \tag{3}$$

In the previous equations several non-dimensional parameters were defined in terms of the inertia tensor of the cylinder I, the distance between the center of mass of the cylinder and the fixed point h, the spring stiffness k, the gravitational acceleration g, and the dissipation constants in the two angular directions α_i of the mast. The reduced mass of the system $m_r^* = [I/(dh)]/[\pi(d/2)^2 l\rho_f]$ compares the mass of fluid displaced by the cylinder with its moment of inertia, and acts as an effective mass of the system; in a similar way, the non-dimensional parameter $m_{gr}^* = u_0^2 I/(mgd^2h)$ compares the influence of the gravity potential energy of the mast with the kinetic energy provided by the flow. The reduced velocity $u_r^* = 2\pi u_0/[\sqrt{k/(I/h^2)}\,d]$ is the inverse of the natural frequency of the system scaled by the factor u_0/d. The damping forces are represented with the non-dimensional parameter $\zeta_i^* = \alpha_i/(2\sqrt{kI/h^2})$.

The forces of the fluid on the structure are of the form $F_i = \frac{1}{2}\rho_f\, u_0^2 C_i A$, where the subindex i represents x, y or z, and C_i is the force coefficient in the corresponding direction. The reference surface $A = dl$ is used with l the length of the mast. In the present work, the potential energy parameter is considered to be negligible $m^*_{gr} = 0$, and a small value of the mass damping ratio $4\pi\zeta^*_i/u^*_r = 0.01$ is used in each direction.

3. Numerical formulation

The FSI numerical scheme of the Alya code, developed at the Barcelona Supercomputing Center was used in the present work. The Navier-Stokes equations were discretized using the stabilized finite element method with Variational MultiScale stabilization. The momentum equation is separated from the continuity equation using the Schur complement for the pressure, each equation is solved independently and the solution of the coupled system is obtained in an iterative way. The time integration scheme used is a backward differentiation formula of second order. A variable time step of order $\mathcal{O}(10^{-3})$ was used, which when reduced by a factor four did not produce noticeable changes in the numerical solution. The details and validation of the solution strategy for the Navier-Stokes equations are provided in [17, 18]. The rigid body equations were integrated in time using a fourth order Runge-Kutta method. Similar set-ups were used for a previous pivoted cylinder study in [12] and for an elastically mounted cylinder in turbulent regime in [10].

In the present work, a loosely coupled algorithm is employed. In one time step, the fluid mechanics problem is solved, the hydrodynamic forces on the cylinder are calculated and used to solve the rigid body equations; with the new location of the rigid body, the fluid mesh is moved and the time step is advanced. The same numerical strategy was used in the same kind of simulations in [12].

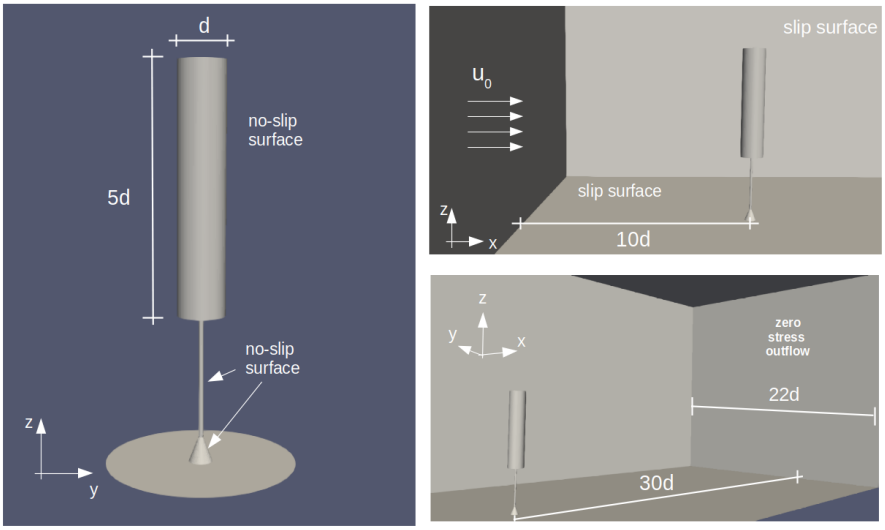

Figure 2: Domain size and boundary conditions scheme.

3.1. Boundary conditions and mesh properties

The boundary conditions imposed in the present work follow. A uniform velocity flow of magnitude u_0 is imposed at the inflow. Slip boundary conditions are imposed at the bottom, top, and sidewalls of the box. Non-slip boundary conditions are imposed at the cylinder, the thin bar, and the base. See Fig.2.

The meshes are constructed aiming to obtain a good balance between the accuracy of the numerical solution, and the number of elements of the grid. In order to do so, a plane cut perpendicular to the cylinder is meshed, and extruded along the cylinder length. The extrusion is done with a space between successive planes of $0.12d$. The mesh of the plane is done clustering elements near the cylinder surface, a distance of $0.09d$ from this surface is covered with four layers of elements to solve correctly the boundary layer. The rest of the box is meshed with tetrahedral elements, obtaining meshes within the range 1M-1.4M elements for different aspect ratios. The meshes were generated using the pre-processing tool ANSA, from BETA-CAE Systems.

The simulations were run using three supercomputing facilities: Nord3 at Barcelona Supercomputing Center; Miztli at 'Universidad Nacional Autónoma de México'; and Hipatia, the local cluster at 'Escuela Nacional de Estudios Superiores, unidad Mérida'. The number of cores used for different cases were in the range 40-80, and a typical simulation was completed within 60 hours.

In order to assess on the grid sensitivity of the numerical solution, the case with $AR = 5$ and $u_r^* = 6$ with $m_r^* = 5$, which has a large amplitude of oscillation and a relatively high frequency, was simulated using three different computational meshes. The first mesh has 700K elements, the second one 1.1M elements, and the third one 3M elements. The refinements were done in the size of the elements on the plane, and the number of planes used in the extrusion. The maximum difference on the mean and RMS value of the oscillation amplitudes between the second and third meshes is less than 2%, and the maximum difference in the mean and RMS values of the force coefficients is less than 6%. Thus, the 1.1M elements mesh is considered adequate to accurately solve the proposed problem.

4. Numerical results

The interaction between the flow and the moving cylinder causes deviations from the vertical in the axis of the mast, which bends in the direction of the flow. Depending on the reduced velocity, different oscillation amplitudes are observed, giving rise to the well-known three branches response described for similar 2dof systems in the literature (e.g. [12, 10, 19]). An initial branch, where the VIV is triggered; an upper branch, where the largest amplitude oscillations are registered; and a lower branch, where the amplitude decreases and after wich synchronization is finally lost.

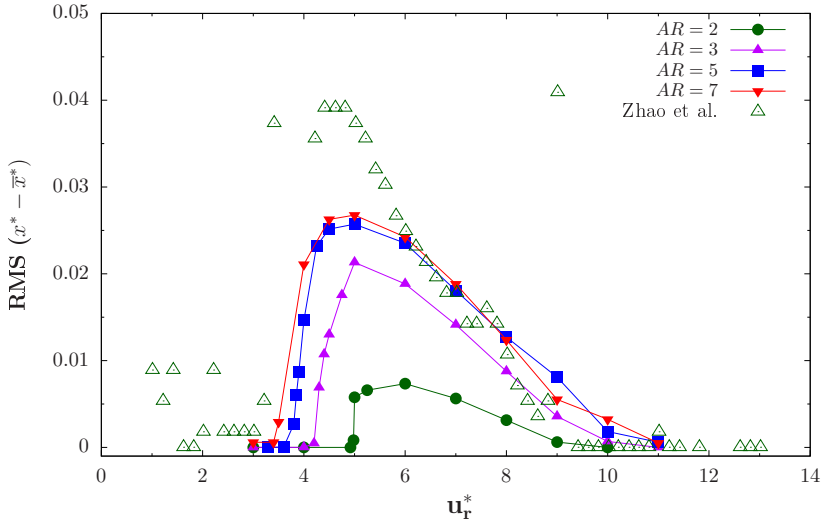

Figure 3: RMS value of amplitude in x^*-direction around $\overline{x}$ for the last ten oscillation cycles in the cross-flow direction. Numerical results of the laminar case of Zhao et al.[19] are included as reference.

4.1. Aspect ratio influence on the maximum oscillation amplitude

The differences due to the aspect ratio in the maximum oscillation amplitude of the center of mass of the cylinder can be observed in Figs.3, and 4. The figures show the RMS values for the oscillations in the x^*-direction around the mean value $\bar{x}^*$, and in the y^*-direction. In both cases, it is notorious that the maximum RMS values for the amplitudes are significantly smaller for aspect ratios $AR = 2$, 3 (with lowest values for $AR = 2$), and become very similar for $AR = 5$, 7. Numerical results for similar systems are included in the figures as reference. The results from Zhao et al.[19] for a 2dof ellasticaly mounted cylinder with $Re = 150$ and $m_r^* = 2$, and Bourguet and Lo Jacono (B&LJ) for a 1dof ellasticaly mounted case with $Re = 100$ and structure/fluid mass ratio of 10 are selected. It is pointed out that the magnitude differences observed in the figures are due to the RMS values in the present study being calculated using the center of mass of the cylinders.

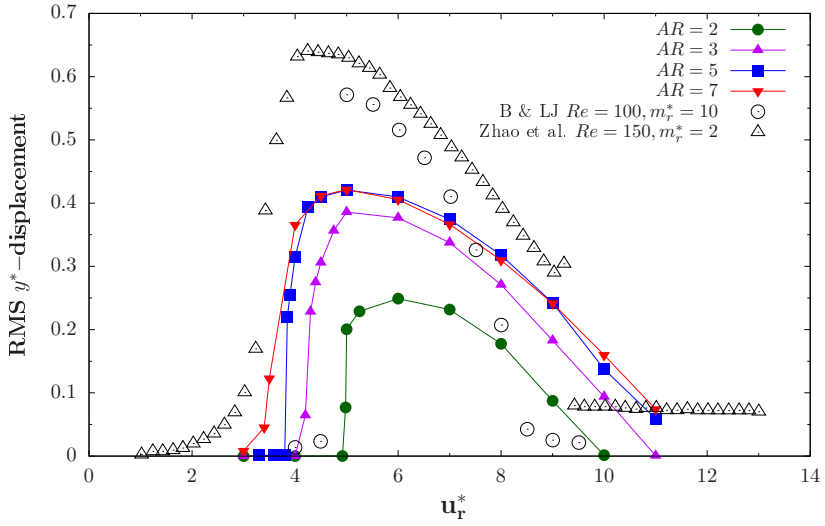

Figure 4: RMS value of amplitude in y^*-direction for the last ten oscillation cycles in the cross-flow direction. Numerical results of laminar cases of B&LJ[20] and Zhao et al.[19] are included as references.

At this point it is convinient to remember the analytical solution for the amplitude in the classical driven-damped oscillator, which matches quite well the present system for small inclination angles of the mast, as shown in [12]. The corresponding solution is

$$\Theta_m = \frac{F_{xm}}{\sqrt{(\omega_0^2 - \omega_x^2)^2 + \omega_x^2 \beta_x^2}} \tag{4}$$

and

$$\Phi_m = \frac{F_{ym}}{\sqrt{(\omega_0^2 - \omega_y^2)^2 + \omega_y^2 \beta_y^2}}, \tag{5}$$

where Θ_m and Φ_m are the amplitudes of the angular displacements, the forcing fluctuation magnitudes are F_{xm} and F_{ym}, the forcing frequencies are ω_x and ω_y, the nondimensional natural frequency of the system is ω_0, and β_x and β_y are damping parameters.

In view of the analytical solution, large differences in the angular oscillation amplitudes are expected to be mainly due to different forcing frequencies, or to

important differences in forcing fluctuations magnitudes. In order to compare the effect of the AR in these quantities, Tables 1 and 2 show the RMS values of the forcing magnitudes and the forcing frequencies in the x^* and y^*-direction for selected values of u_r^*, and all AR analyzed. Comparing the frequencies of the larger oscillation amplitudes cases, it is observed that $AR = 2$ has significantly smaller values than those for $AR = 3, 5, 7$, with maximum differences of 13% in both directions. Comparing the cases with $AR = 3$ against $AR = 5, 7$ the differences are still noticeables, but smaller, with a maximum difference of 7.4% in the in-line direction and 10% in the cross-flow direction. The cases with $AR = 5, 7$ have very similar forcing frequencies and amplitudes. Thus, the response of the cylinder is very similar in both cases when large amplitude oscillations are present.

The forcing fluctuations magnitudes for the large amplitude cases follow a similar trend. Large differences between $AR = 2$ and the other cases are observed, with less notorious differences as AR increases. It is important to mention that the maximum oscillation amplitude does not necessarily coincide with the maximum value of the forcing fluctuations, and is also dependent of the u_r^* value.

Tables 1 and 2 also show that the forcing frequencies for fixed values of u_r^* increase with AR, reaching very similar values for $AR = 5, 7$. This is in good agreement with the results published in [13], where a noticeable variation of the Strouhal number (due to vortex shedding) for small AR fixed cylinders is reported, with values around $St = 0.10$ for $AR = 5$ and values around $St = 0.125$ as AR approaches 10. These values compare very well with the Strouhal numbers in the y^*-direction obtained for the very small amplitude cases: $St = 0.097$ for $u_r^* = 3$ and $AR = 5$; and $St = 0.111$ for $u_r^* = 3$ and $AR = 7$ (see Table 2).

	$AR = 2$	$AR = 3$	$AR = 5$	$AR = 7$
u_r^* $[\omega_o/2\pi]$	C_{xrms} $[\omega_x]$	C_{xrms} $[\omega_x]$	C_{xrms} $[\omega_x]$	C_{xrms} $[\omega_x]$
3 [0.333]	$\mathcal{O}(10^{-5})$ [−−]	$\mathcal{O}(10^{-4})$ [−−]	$\mathcal{O}(10^{-4})$ [−−]	0.001 [−−]
4 [0.250]	$\mathcal{O}(10^{-4})$ [−−]	$\mathcal{O}(10^{-4})$ [−−]	0.034 [0.296]	0.034 [0.323]
5 [0.200]	0.014 [0.257]	0.067 [0.274]	0.095 [0.292]	0.102 [0.296]
6 [0.166]	0.022 [0.232]	0.060 [0.250]	0.083 [0.260]	0.083 [0.265]
7 [0.143]	0.018 [0.213]	0.044 [0.227]	0.057 [0.233]	0.060 [0.237]
8 [0.125]	0.009 [0.192]	0.026 [0.208]	0.038 [0.212]	0.038 [0.219]
9 [0.111]	0.002 [0.182]	0.012 [0.188]	0.020 [0.195]	0.022 [0.203]
10 [0.100]	$\mathcal{O}(10^{-6})$ [−−]	0.005 [0.187]	0.006 [0.185]	0.010 [0.192]

Table 1: RMS value of force coefficient in x^*-direction C_{xrms}, for the last ten oscillation cycles in the quasi-periodic state for different aspect ratios.

	$AR = 2$	$AR = 3$	$AR = 5$	$AR = 7$
u_r^* $[\omega_o/2\pi]$	C_{yrms} $[\omega_y]$	C_{yrms} $[\omega_y]$	C_{yrms} $[\omega_y]$	C_{yrms} $[\omega_y]$
3 [0.333]	0.002 [−−]	$\mathcal{O}(10^{-4})$ [−−]	0.007 [0.097]	0.028 [0.111]
4 [0.250]	0.004 [−−]	$\mathcal{O}(10^{-4})$ [0.145]	0.779 [0.147]	0.838 [0.159]
5 [0.200]	0.288 [0.130]	0.495 [0.135]	0.470 [0.143]	0.445 [0.150]
6 [0.166]	0.209 [0.118]	0.268 [0.125]	0.258 [0.131]	0.236 [0.130]
7 [0.143]	0.120 [0.110]	0.142 [0.113]	0.135 [0.116]	0.119 [0.118]
8 [0.125]	0.061 [0.097]	0.066 [0.103]	0.068 [0.107]	0.052 [0.106]
9 [0.111]	0.016 [0.091]	0.020 [0.091]	0.025 [0.097]	0.015 [0.104]
10 [0.100]	$\mathcal{O}(10^{-4})$[0.083]	0.007 [0.095]	0.007 [0.092]	0.003 [0.094]

Table 2: RMS value of force coefficient in y^*-direction C_{yrms}, for the last ten oscillation cycles in the quasi-periodic state for different aspect ratios.

4.2. Aspect ratio influence on the extent of the synchronization region

Figures 3, and 4 show that the beginning of the initial branch (IB) depends strongly on the AR value. The effect is specially notorious in the case $AR = 2$, where the IB starts between the values $u_r^* = 4.92, 4.98$; for $AR = 3$ the beginning of the IB is between the values $u_r^* = 4, 4.3$; for $AR = 5$ the IB starts between $u_r^* = 3.8, 3.85$; and for $AR = 7$ the beginning of the IB is between $u_r^* = 3, 3.4$. It is pointed out that the IB starts earlier for cylinder with larger AR in all studied cases. Also, it is observed that the decay in the oscillation amplitudes is affected by AR. For $AR = 2$ extremely small amplitude oscillations are registered when $u_r^* = 10$, while for $AR = 3$ small but noticeable oscillations are obtained for this same value of the reduced velocity, obtaining extremely small oscillations when $u_r^* = 11$; for $AR = 5, 7$ small amplitude oscillations are still registered for $u_r^* = 11$, and both cases follow very similar decaying trends as u_r^* increases.

The above results show that cylinders with large AR are able to oscillate over a wider range of reduced velocities than those with smaller AR. For the parameters analyzed, the authors noticed that a relatively large $AR = 5, 7$ makes it possible to create two different wake structures with different shedding frequencies depending on the oscillation amplitudes. It is the authors' affirmation that this is the reason why AR influences the extent of the synchronization region, and also this is the reason why this influence is less notorious for increasing AR, where two kind of vortex streets are obtained. Section 4.3 describes further these wake structures.

4.3. Wake structures dependence on AR and oscillation amplitude

The wake structures obtained in the present study include a stationary flow (referred to as continous shedding by some authors), hairpin vortices that form closed loops alternately detached from opposing sides of the cylinder (see for example 5a), and vortex streets that result from the dislocations and reconnections between vortices shed from opposite sides of the cylinder (see for example 5d).

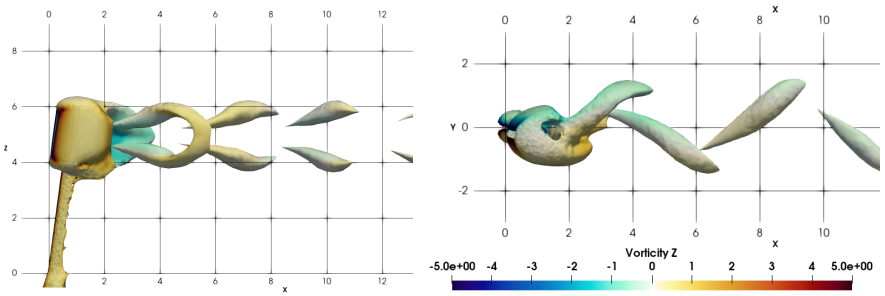

(a)

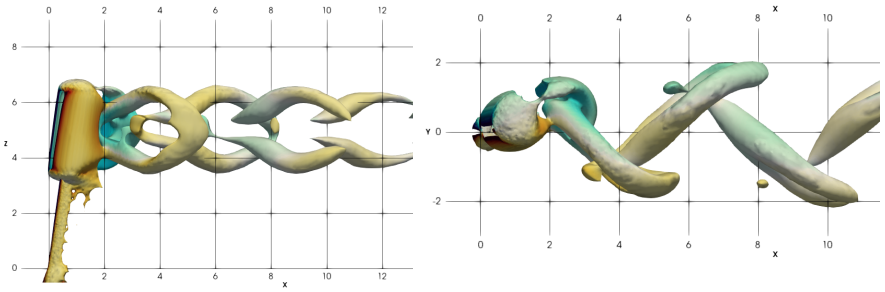

(b)

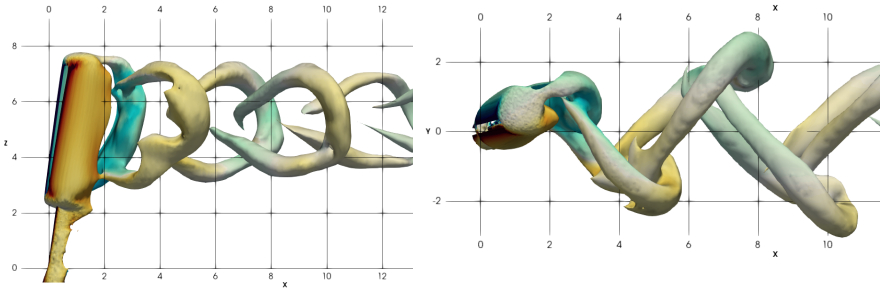

(c)

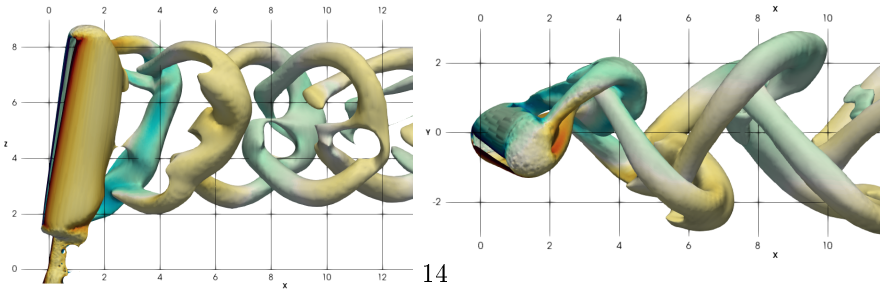

(d)

Figure 5: Lateral view (left) and top view (right) of the vortical structures shown by instantaneous Q iso-surfaces, $Q = 0.05u_0^2/d^2$ colored by the vorticity in z^*-direction for the largest amplitude oscillating cases for (a) $AR = 2$, $u_r^* = 5$ (b) $AR = 3$, $u_r^* = 5$ (c) $AR = 5$, $u_r^* = 5$ (d) $AR = 7$, $u_r^* = 5$

The shedding process and the characteristics of the latter have been described in detail in [12] and will not be repeated here. To contribute the comparisons between the AR values of the cylinder, it will only be pointed out that for sufficiently large values of AR the shedding process is done out of phase along the cylinder axis. The shedding starts from top to bottom with enough separation to facilitate vortex dislocations and reconnections. The cylinders with small $AR = 2, 3$ do not show both wake configurations, and only hairpin vortices were obtained for all values of u_r^* in the present study. Figure 5 also shows that the vertical size of the coherent structures is similar to, but slightly smaller than the AR value. The width of the wake broadens as the oscillation amplitude increases, ranging from d for small amplitude cases, to $6d$ for large amplitude ones. It is pointed out that these kind of wake structures for finite length fixed cylinders are described in detail in [13].

The continuous shedding wake was obtained for $AR = 2, 3$ cases with values of $u_r^* < 4.98$ for the first and $u_r^* < 4.3$ for the second. This is in good agreement with the numerical results reported in [13], where no asymmetrical shedding was observed for this values of AR and $Re = 100$. The presence of asymmetrical shedding and noticeable amplitude oscillations for larger values of u_r^* reveals that this wake configuration is not stable in the movable cylinder case. This point will be further discussed in subsection 4.4.

The hairpin vortices were not observed in [12] due to the relatively large AR value used in that work. Thus, more details on the shedding process of this pattern will be presented. Fig. 6 show three instants of the shedding process for half a cycle in the y^*-direction in units of the oscillation period τ for the case with $u_r^* = 5$ (large amplitude) for $AR = 2$. Fig.6a shows the beginning of the cycle at 0τ when the maximum displacement in the negative y^*-direction is observed, the roll-up of the shear layer has occured and remains attached to the left side of the cylinder; then at 0.28τ (Fig.6b), the separation of the coherent structure from the shear layer takes place as the cylinder displaces in the pos-

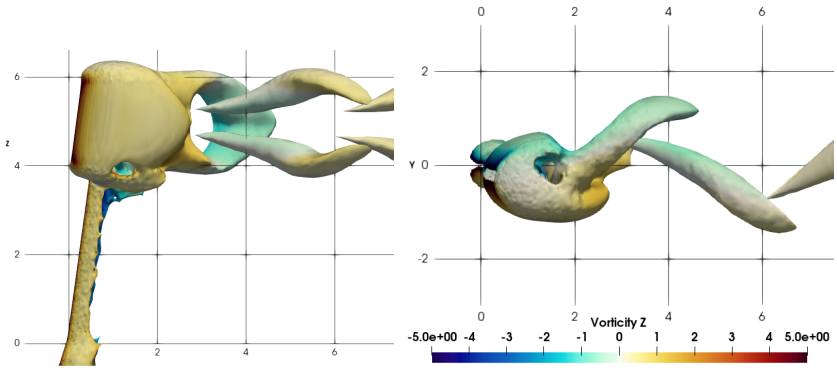

(a)

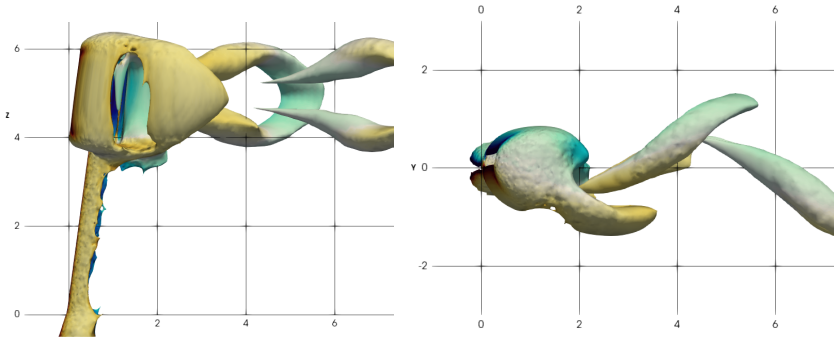

(b)

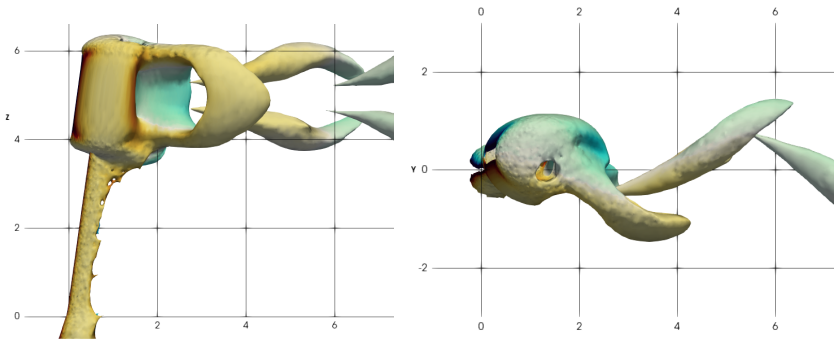

(c)

Figure 6: Lateral view (left) and top view (right) of the vortical structures shown by instantaneous Q iso-surfaces, $Q = 0.05u_0^2/d^2$ colored by the vorticity in z^*-direction for $AR = 2$, $u_r^* = 5$, for half a cycle in y^*-direction, (a) 0τ (b) 0.3τ, (c) 0.45τ

itive y^*-direction; approaching the half cycle at 0.46τ the vortex has separated almost completely from the shear layer and is shed into the wake. It is very important to notice that, given the relatively short distance between the top and bottom ends of the cylinder, the shedding process does not show a heavy out of phase behaviour, as with the large AR cylinders. Thus, no vortex dislocations and reconnections were observed.

The different wake structures that can be obtained depending on the values of u_r^* in the relatively large $AR = 5$ cylinders are illustrated in Fig. 7. First, a hairpin vortex street is obtained for a very small amplitude oscillating case with $u_r^* = 3.8$, an interconnected vortex street is present for the large amplitude case $u_r^* = 5$, and an elongated version of the hairpin vortices structure is observed for another small amplitude case with $u_r^* = 10$. As expected, the deviation of the axis of the cylinder from the vertical increases as the u_r^* values increase. From this figure, it is clear that increasing AR makes it possible to generate the required separation to obtain vortex dislocations and reconnections.

4.4. FSI breaks symmetry of the wake in small AR cases

Small values of Re combined with small values of AR produce the steady shedding of counter-rotating vortex pairs [13]. The cases of $Re = 100$ and $AR = 2, 3$ fall in this type of flow. Two instants of time for the wake corresponding to $AR = 2$ and $u_r^* = 3$ are shown in Fig.8. Initially, there are two vortical structures being shed continuously from opposite sides of the cylinder (Fig. 8a). When the flow fully develops, a symmetrical and steady state is obtained (Fig. 8b). This wake structure does not produce oscillating forces, and in consequence no oscillations of the cylinder are registered for $u_r^* < 4.98$ when $AR = 2$, and for $u_r^* < 4.3$ when $AR = 3$.

The presence of noticeable oscillations, accompanied with the hairpin wake structure, for cases with $AR = 2, 3$ indicates that the symmetric shedding obtained for fixed cases [13], and for the named values of u_r^* is not preserved as

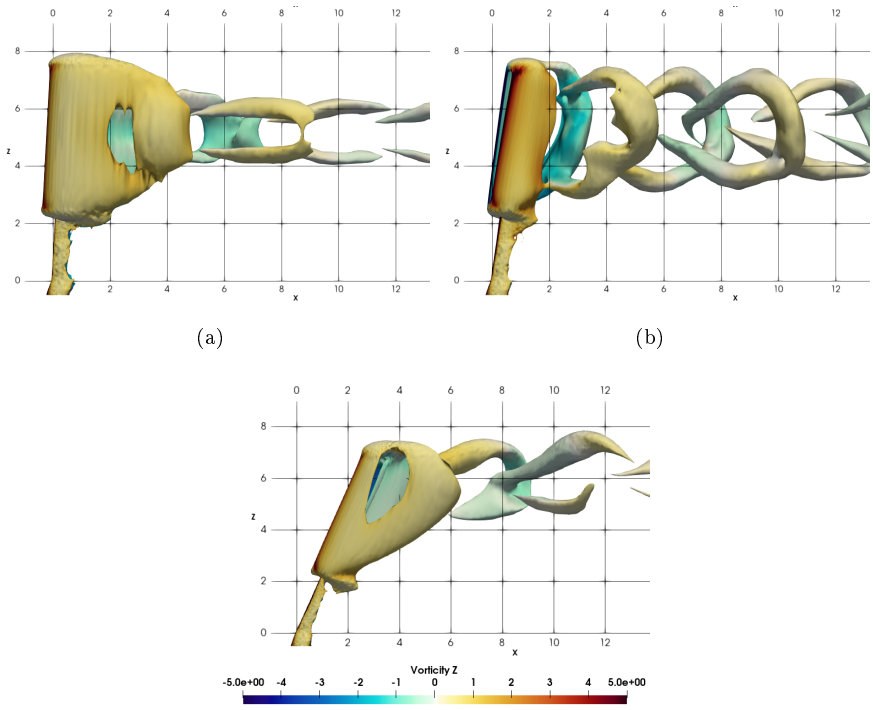

Figure 7: Lateral view of the vortical structures shown by instantaneous Q iso-surfaces, $Q = 0.043u_0^2/d^2$ colored by the vorticity in z^*-direction for $AR = 5$ and (a)$u_r^* = 3.8$, (b) $u_r^* = 5$, and (c) $u_r^* = 10$.

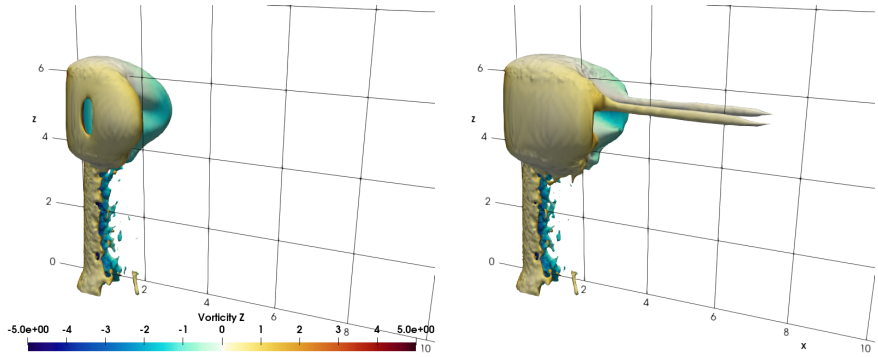

(a) (b)

Figure 8: Vortical structures shown by instantaneous Q iso-surfaces, $Q = 0.01u_0^2/d^2$ colored by the vorticity in z^*-direction for $AR = 2$ and $u_r^* = 3$, (a) initial stage of the shedding process, (b) fully developed steady state flow.

u_r^* increases further. Considering the differences between the fixed and mobile cases, two possible reasons arise for this symmetry breaking: first, larger values of u_r^* provoke larger inclination angles that could induce asymmetry in the flow by geometric considerations; second, large values of u_r^* create a physically unstable FSI symmetrical configuration due to the variations in the natural frequency of the moving cylinder. In order to shed ligth on this symmetry breaking process, a simulation with an inclined fixed cylinder with $AR = 2$ and $Re = 100$ was performed. The inclination angle was chosen to be sligthly larger than the average inclination angle of the case $AR = 2$, $u_r^* = 4.98$, which is the first to show noticeable oscillations for this value of AR.

Figure 9 shows a comparison between the pressure contours and the y^*-direction vorticity field of the fixed inclined case and the $u_r^* = 4.98$ case. It is observed in Fig.9a that the recirculation regions in the upper and lower ends of the cylinder are similar in size to d, and therefore are very close to each other. A strong interaction between both recirculation regions is obtained and the relative high pressure zone at the rear of the cylinder is completely enclosed by contours

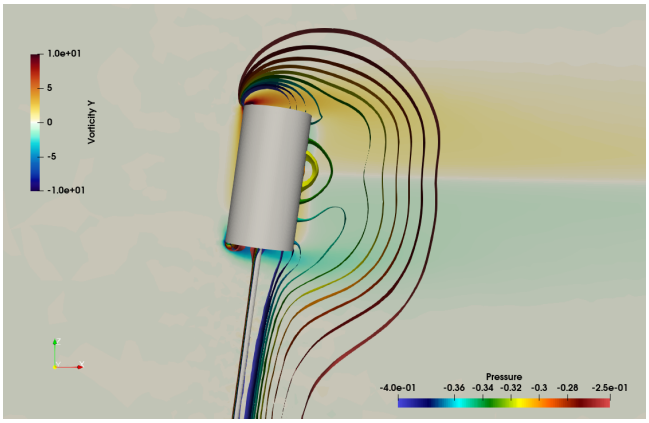

(a)

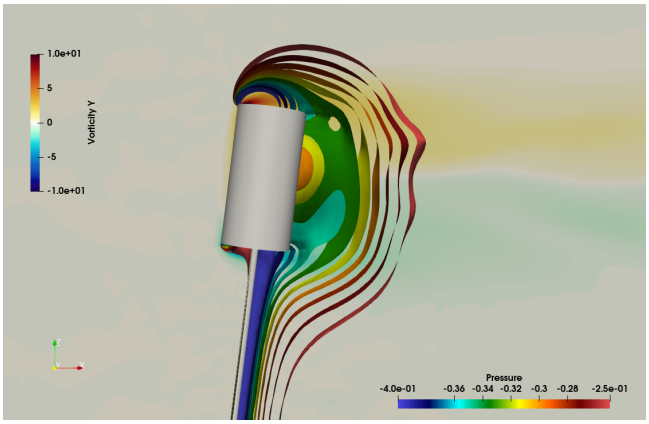

(b)

Figure 9: Pressure contours and vorticity field in the y^*-direction for $AR = 2$ (a) inclined fixed cylinder, (b) $u_r^* = 4.98$.

of constant pressure that form smooth and closed surfaces. The inclination angle deviates the named relative high pressure zone towards the top of the cylinder, but in this case this deviation is not enough to induce an asymmetric shedding pattern. The case with $u_r^* = 4.98$ show similar characteristics, but the constant pressure countours show humps that together with the undulating shape of the vorticity field reveals the presence of asymmetric shedding. These results indicate that the asymmetric shedding pattern is linked to the physical onset defined by the values of u_r^*, and not just to the geometric configuration induced by the inclination angle. Further research in this particular aspect is then suggested for future work.

5. Conclusions

The effect of the aspect ratio on the VIV of a pivoted finite length circular cylinder has been investigated. A fixed value of the Reynolds number $Re = 100$ was used with four values of $AR = 2, 3, 5, 7$; different values of the reduced velocity u_r^* in the range $2 \leq u_r^* \leq 11$ were considered for each analyzed value of AR. Results on the oscillatory response, hydrodynamic forces, and wake structures were obtained. In order to compare the VIV of the different length cylinders, the displacement of the center of mass (which coincides on each case) was analyzed. The main conclusions of the present work follow.

The RMS values of oscillation amplitudes in both directions (around its mean values) were found to be strongly influenced by the AR value for cases with $AR = 2, 3$, and to follow very similar trends for the larger values $AR = 5, 7$. These differences are mainly due to the dependence of the forcing frequency (vortex shedding) on the AR parameter, which is stronger for small AR, and tends to a limiting value as AR increases. Also, the magnitude of the hydrodynamic forces follow a similar behaviour, with a strong dependence on AR for small values $AR = 2, 3$ and reaching a limiting value as AR increases.

The extent of the synchronization region and the wake structures obtained were also found to be dependent on the AR value. A very pronounced effect is obtained for $AR = 2$, 3, where steady symmetrical vortex shedding is obtained for $u_r^* < 4.98$ in the case $AR = 2$, and for $u_r^* < 4.3$ in the case $AR = 3$, causing a very narrow synchronization window in the u_r^* considered values. The extent of the synchronization region is considerably larger for $AR = 5, 7$ than for $AR = 2$, 3, but less notorious differences are obtained comparing $AR = 5$ with $AR = 7$. When obtaining periodic shedding, the small AR cylinders show hairpin vortices wakes, while cylinders with $AR = 5$, 7 show hairpin vortices and connected vortex streets obtained from vortex dislocations and reconnections. It is the authors' affirmation that the ability to produce different vortex shedding patterns of the larger AR cylinders is the reason why the extent of the synchronization region varies as described.

The symmetry of the mentioned steady shedding for $AR = 2$, 3 is broken when increasing the u_r^* value. The results of section 4.4 suggest that this symmetry break is due to an unstable FSI physical onset, and not to the larger inclination angles obtained when increasing u_r^*. Further investigation is needed to draw definite conclusions on this point.

Acknowledgments

J.C. Cajas acknowledges the financial support of UNAM DGAPA through the project PAPIIT-IA106120; the access to supercomputing resources at Miztli through the project LANCAD-UNAM-DGTIC-379, and at Hipatia through the project CONACyT-CF21088; the technical support of Joaquín Morales ('Departamento de Matemáticas Aplicadas y Computación' ENES Mérida) is also acknowledged.

AIP DATA SHARING POLICY

The data that support the findings of this study are available from the corresponding author upon reasonable request.

References

[1] T. Sarpkaya, A critical review of the intrinsic nature of vortex-induced vibrations, Journal of Fluids and Structures 19 (4) (2004) 389–447. doi:10.1016/j.jfluidstructs.2004.02.005.

[2] C. H. K. Williamson, R. Govardhan, A brief review of recent results in vortex-induced vibrations, Journal of Wind Engineering and Industrial Aerodynamics 96 (6-7) (2008) 713–735. doi:10.1016/j.jweia.2007.06.019.

[3] P. W. Bearman, Circular cylinder wakes and vortex-induced vibrations, Journal of Fluids and Structures 27 (5-6) (2011) 648–658. doi:10.1016/j.jfluidstructs.2011.03.021.
URL http://dx.doi.org/10.1016/j.jfluidstructs.2011.03.021

[4] Y. Bazilevs, K. Takizawa, T. E. Tezduyar, Front Matter, in Computational Fluid-Structure Interaction: Methods and Applications, John Wiley & Sons, Ltd, Chichester, UK, 2013. doi:10.1002/9781118483565.fmatter.

[5] T. Richter, Fluid-structure Interactions, Vol. 118 of Lecture Notes in Computational Science and Engineering, Springer International Publishing, 2017. doi:10.1007/978-3-319-63970-3.

[6] A. Khalak, C. H. K. Williamson, Fluid Forces And Dynamics Of A Hydroelastic Structure With Very Low Mass And Damping, Journal of Fluids and Structures 11 (8) (1997) 973–982. doi:10.1006/jfls.1997.0110.
URL http://www.sciencedirect.com/science/article/pii/S0889974697901109

[7] N. Jauvtis, C. H. K. Williamson, The effect of two degrees of freedom on vortex-induced vibration at low mass and damping, Journal of Fluid Mechanics 509 (2004) 23–62.

[8] S. Gsell, R. Bourguet, M. Braza, Two-degree-of-freedom vortex-induced vibrations of a circular cylinder at Re=3900, Journal of Fluids and Structures 67 (2016) 156–172.

[9] D. Lo Jacono, R. Bourguet, M. C. Thompson, J. S. Leontini, Three-dimensional mode selection of the flow past a rotating and inline oscillating cylinder, Journal of Fluid Mechanics 855 (2018) 1–11. doi:10.1017/jfm.2018.700.

[10] D. Pastrana, J. Cajas, O. Lehmkuhl, I. Rodríguez, G. Houzeaux, Large-eddy simulations of the vortex-induced vibration of a low mass ratio two-degree-of-freedom circular cylinder at subcritical Reynolds numbers, Computers & Fluids 173 (2018) 118–132. doi:https://doi.org/10.1016/j.compfluid.2018.03.016.

[11] R. Bourguet, Two-degree-of-freedom flow-induced vibrations of a rotating cylinder, Journal of Fluid Mechanicsdoi:10.1017/jfm.2020.403.

[12] J. C. Cajas, D. Pastrana, I. Rodríguez, O. Lehmkuhl, G. Houzeaux, M. Vázquez, C. Treviño, Vortex induced vibrations of a pivoted finite height cylinder at low Reynolds number, Physics of Fluids 33 (6) (2021) 063602. doi:10.1063/5.0051689.

[13] O. Inoue, A. Sakuragi, Vortex shedding from a circular cylinder of finite length at low Reynolds numbers, Physics of Fluids 20 (2008) 033601. doi:10.1063/1.2844875.

[14] J. L. Pierson, F. Auguste, A. Hammouti, A. Wachs, Inertial flow past a finite-length axisymmetric cylinder of aspect ratio 3: Effect of the yaw angle, Physical Review Fluids 4 (4) (2019) 044802. doi:10.1103/PhysRevFluids.4.044802.

[15] M. Zhao, L. Cheng, Vortex-induced vibration of a circular cylinder of finite length, Physics of Fluids 26 (1) (2014) 015111. doi:10.1063/1.4862548.

[16] V. Azadeh-Ranjbar, N. Elvin, Y. Andreopoulos, Vortex-induced vibration of finite-length circular cylinders with spanwise free-ends: Broadening the lock-in envelope, Physics of Fluids 30 (10) (2018) 105104. doi:10.1063/1.5042774.
URL http://dx.doi.org/10.1063/1.5042774

[17] G. Houzeaux, J. Principe, A variational subgrid scale model for transient incompressible flows, Int. J. CFD 22 (3) (2008) 135–152.

[18] G. Houzeaux, R. Aubry, M. Vázquez, Extension of fractional step techniques for incompressible flows: The preconditioned orthomin(1) for the pressure schur complement, Computers & Fluids 44 (1) (2011) 297–313.

[19] M. Zhao, L. Cheng, L. Lu, Vortex induced vibrations of a rotating circular cylinder at low Reynolds number, Physics of Fluids 26 (7) (2014) 073602. doi:10.1063/1.4886196.
URL http://aip.scitation.org/doi/10.1063/1.4886196

[20] R. Bourguet, D. Lo Jacono, Flow-induced vibrations of a rotating cylinder, Journal of Fluid Mechanics 740 (4) (2014) 342–380. doi:10.1017/jfm.2013.665.